JOURNAL OF THERMOPHYSICS AND HEAT TRANSFER
Vol. 7, No. 2, April–June 1993

Investigation of the Temporal Thermal Performance of the Wheel Outboard of an Aircraft

C. P. Desai* and K. Vafai†
Ohio State University, Columbus, Ohio 43210

Three-dimensional transient natural convection flow and heat transfer around the wheel outboard portion of an aircraft brake housing was investigated. The wheel outboard is modeled as an annular cavity with one end open to the ambient surroundings. The temporal development of the flow and temperature fields and its effect on the thermal performance of the brake housing outboard is discussed. The transient results are presented here by means of the velocity and temperature fields and the average Nusselt numbers over the different surfaces of the geometry. The effect of Rayleigh number and length of the inner cylinder on the thermal performance of the wheel outboard are also discussed.

Nomenclature

F = force vector of the unknown variables
K = stiffness matrix (representing the diffusion and convection of energy)
L_1 = length of the inner cylinder
L_2 = length of the outer cylinder
L_3 = length of the extended computational domain
M = mass matrix
Nu = Nusselt number, defined in Eq. (16)
n = outward normal to a surface
Pr = Prandtl number, ν/α
p = pressure
Ra = Rayleigh number, $g\beta R_2^3 \Delta T/\nu\alpha$
R_1 = radius of the inner cylinder
R_2 = radius of the outer cylinder
R_3 = radius of the extended computational domain
r, θ, z = cylindrical coordinates
T = temperature
T_∞ = reference (ambient) temperature
t = time
u_r, u_θ, u_z = r, θ, z components of velocity
V = column vector consisting of all the unknown variables in the computational domain $(u_r, u_\theta, u_z, p, T)$
α = thermal diffusivity
μ = dynamic viscosity

I. Introduction

THE wheel outboard of the brake housing of an aircraft shown in Fig. 1, can be modeled as an annular cavity with one end open to the ambient surroundings. Thus, the thermal performance of the wheel outboard can be assessed by studying the complex, transient three-dimensional process of natural convection in a partially open annular cavity.

Three-dimensional numerical studies have been made on the buoyancy induced flow and heat transfer in an annulus with closed end walls.[1–3] However, the even more interesting phenomenon of buoyancy driven flow in an annular cavity with an open end has only recently received some attention. The buoyancy induced flow in a partially open cavity is characterized by the complex interactions betwen the inner and outer flow and temperature fields. There has been very little work on these types of interactions which can occur in various practical applications.

The wheel outboard portion of an aircraft brake housing is a direct application of this geometry. When an aircraft lands, the brakes (which are usually of the disc-type) are applied. Because of the considerable amount of kinetic energy that has to be dissipated as friction, the amount of heat generated in the brake assembly is quite large. The real cooling process begins after the aircraft comes to a halt, because the time interval between the application of the brakes and the aircraft becoming stationary is relatively small. The brake housing assembly partly interacts with the surroundings through the wheel outboard portion. The axle becomes hot, and since it extends into the wheel outboard portion of the assembly, causes natural convection currents to be set up in this region. This is responsible for the cooling of the brake assembly in the absence of any artificial means in the "ambient" sur-

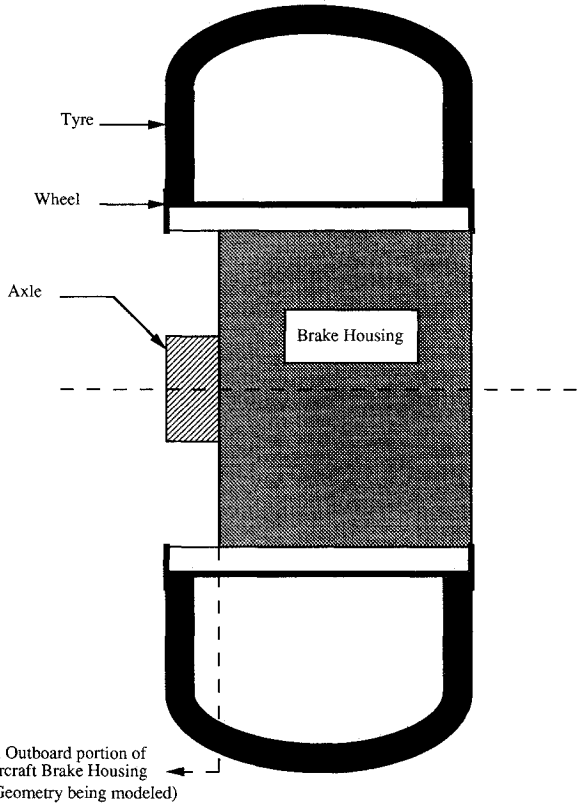

Fig. 1 Schematic sketch of the brake housing assembly of an aircraft.

Received Sept. 3, 1991; revision received March 9, 1992; accepted for publication March 12, 1992.

*Graduate Research Associate, Department of Mechanical Engineering.
†Professor, Department of Mechanical Engineering.

roundings when the aircraft is stationary. Therefore, the axle tip is the hot inner cylinder in the model and it is the part that dissipates heat to the surroundings from the inner parts of the brake housing. It is the above-mentioned process which has been modeled in the present work. The annular cavity of interest here is the portion between the axle tip and the wheel rim on which the tire is mounted. A thorough understanding of the natural convection process in this geometry provides a strong basis for evaluating and optimizing the thermal performance of the outboard of the brake housing assembly.

The main difficulty associated with the study of fluid flow and heat transfer effects in open-ended structures is the specification of boundary conditions at the open end. It has been shown,[4,5] that the extent of the enlarged computational domain has a much more pronounced effect on the results than those anticipated by previous researchers.

This work involves the numerical study of the "transient" three-dimensional flow and heat transfer in a partially open annular cavity which can be used to directly model domains of practical interest such as the wheel outboard of the brake housing of an aircraft. To study the complex interactions between the fluid inside the annular space and that in the ambient surroundings, the boundary conditions at the open end are taken care of by making use of an extended computational domain. The temporal nature of the convective process is emphasized in this work. Transient results depicting the flow and temperature fields are presented here for a typical case. Transient heat transfer results in the form of spatially averaged Nusselt numbers are also presented. The effect of the length of the inner cylinder on the flow and temperature field and the thermal performance of the brake housing is investigated.

II. Analysis

A. Governing Equations

The problem is modeled as a three-dimensional, transient, natural convection flow of an incompressible fluid using the Boussinesq approximation for which the governing equations written in cylindrical coordinates are

$$\frac{1}{r}\frac{\partial}{\partial r}(ru_r) + \frac{1}{r}\frac{\partial u_\theta}{\partial \theta} + \frac{\partial u_z}{\partial z} = 0 \tag{1}$$

$$\left(\frac{Ra}{Pr}\right)^{1/2}\left(\frac{\partial u_r}{\partial t} + u_r\frac{\partial u_r}{\partial r} + \frac{u_\theta}{r}\frac{\partial u_r}{\partial \theta} - \frac{u_\theta^2}{r} + u_z\frac{\partial u_r}{\partial z}\right) = -\frac{\partial p}{\partial r} + \left(\frac{Ra}{Pr}\right)^{1/2} T + \frac{\partial}{\partial r}\left[\frac{1}{r}\frac{\partial}{\partial r}(ru_r)\right] + \frac{1}{r^2}\frac{\partial^2 u_r}{\partial \theta^2} - \frac{2}{r^2}\frac{\partial u_\theta}{\partial \theta} + \frac{\partial^2 u_r}{\partial z^2} \tag{2}$$

$$\left(\frac{Ra}{Pr}\right)^{1/2}\left(\frac{\partial u_\theta}{\partial t} + u_r\frac{\partial u_\theta}{\partial r} + \frac{u_\theta}{r}\frac{\partial u_\theta}{\partial \theta} + \frac{u_r u_\theta}{r} + u_z\frac{\partial u_\theta}{\partial z}\right) = -\frac{1}{r}\frac{\partial p}{\partial \theta} + \frac{\partial}{\partial r}\left[\frac{1}{r}\frac{\partial}{\partial r}(ru_\theta)\right] + \frac{1}{r^2}\frac{\partial^2 u_\theta}{\partial \theta^2} + \frac{2}{r^2}\frac{\partial u_r}{\partial \theta} + \frac{\partial^2 u_\theta}{\partial z^2} \tag{3}$$

$$\left(\frac{Ra}{Pr}\right)^{1/2}\left(\frac{\partial u_z}{\partial t} + u_r\frac{\partial u_z}{\partial r} + \frac{u_\theta}{r}\frac{\partial u_z}{\partial \theta} + u_z\frac{\partial u_z}{\partial z}\right) = -\frac{\partial p}{\partial z} + \frac{1}{r}\frac{\partial}{\partial r}\left(r\frac{\partial u_z}{\partial r}\right) + \frac{1}{r^2}\frac{\partial^2 u_z}{\partial \theta^2} + \frac{\partial^2 u_z}{\partial z^2} \tag{4}$$

$$(RaPr)^{1/2}\left(\frac{\partial T}{\partial t} + u_r\frac{\partial T}{\partial r} + \frac{u_\theta}{r}\frac{\partial T}{\partial \theta} + u_z\frac{\partial T}{\partial z}\right) = \frac{1}{r}\frac{\partial}{\partial r}\left(r\frac{\partial T}{\partial r}\right) + \frac{1}{r^2}\frac{\partial^2 T}{\partial \theta^2} + \frac{\partial^2 T}{\partial z^2} \tag{5}$$

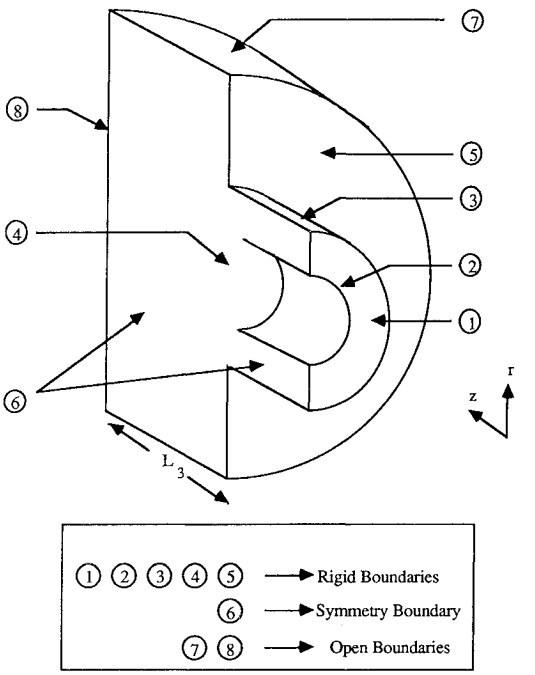

Fig. 2 Extended computational domain used for the present study.

The following nondimensional parameters have been used (for convenience the superscripts were dropped from the above equations):

$$r^* = \frac{r}{R_2}, \quad z^* = \frac{z}{R_2}$$

$$u_r^* = \frac{u_r R_2}{\alpha(RaPr)^{1/2}}, \quad u_\theta^* = \frac{u_\theta R_2}{\alpha(RaPr)^{1/2}}, \quad u_z^* = \frac{u_z R_2}{\alpha(RaPr)^{1/2}}$$

$$T^* = \frac{T - T_\infty}{T_1 - T_\infty}, \quad p^* = \frac{pR_2^2}{\mu\alpha(RaPr)^{1/2}}, \quad t^* = \frac{t\alpha(RaPr)^{1/2}}{R_2^2}$$

where Ra and Pr as well as all the other parameters used are defined in the nomenclature section.

B. Initial Conditions

All the walls of the annulus are assumed to be initially at uniform, ambient temperature, and the fluid is assumed to be stagnant and at the ambient temperature throughout the computational domain. When the aircraft comes to a halt in the ambient surroundings, the air occupying the wheel outboard portion of the assembly can very well be approximated as stagnant and at the ambient temperature. Therefore, the initial conditions being used here relate very closely to the physical situation being modeled in the present study. This boundary condition can be stated as

$$t = 0$$
$$u_r = u_\theta = u_z = T = 0 \tag{6}$$

C. Boundary Conditions

We have made use of an extended computational domain for implementing the virtually unknown boundary conditions at the open end. A sketch of the computational domain for a partially open annular cavity is shown in the Fig. 2. These boundary conditions which have also been discussed by Desai and Vafai[6] are

1) For the axial end wall of the annulus

$$z = 0 \quad \text{and} \quad \frac{R_1}{R_2} \le r \le 1$$
$$u_r = u_\theta = u_z = 0, \quad \frac{\partial T}{\partial z} = 0 \tag{7}$$

2) For the curved surface of the inner cylinder

$$r = \frac{R_1}{R_2} \quad \text{and} \quad 0 \le z \le \frac{L_1}{R_2}$$
$$u_r = u_\theta = u_z = 0, \quad T = T_1 \tag{8}$$

3) For the curved surface of the outer cylinder

$$r = 1 \quad \text{and} \quad 0 \le z \le \frac{L_2}{R_2}$$
$$u_r = u_\theta = u_z = 0, \quad T = T_2 \tag{9}$$

4) For the vertical (flat) surface of the inner cylinder

$$z = \frac{L_1}{R_2} \quad \text{and} \quad 0 \le r \le \frac{R_1}{R_2}$$
$$u_r = u_\theta = u_z = 0, \quad T = T_1 \tag{10}$$

5) For the vertical (flat) surface of the outer cylinder

$$z = \frac{L_2}{R_2} \quad \text{and} \quad 1 \le r \le \frac{R_3}{R_2}$$
$$u_r = u_\theta = u_z = 0, \quad \frac{\partial T}{\partial z} = 0 \tag{11}$$

6) For the symmetry plane

$$u_\theta = 0, \quad \frac{\partial u_r}{\partial \theta} = \frac{\partial u_z}{\partial \theta} = \frac{\partial T}{\partial \theta} = 0 \tag{12}$$

7) For the open radial boundary of the extended computational domain

$$r = \frac{R_3}{R_2} \quad \text{and} \quad 0 \le z \le \frac{L_3 + L_2}{R_2}$$
$$\frac{\partial u_r}{\partial r} = \frac{\partial u_\theta}{\partial r} = \frac{\partial u_z}{\partial r} = 0, \quad \frac{\partial T}{\partial r} = 0 \tag{13}$$

8) For the open axial boundary of the extended computational domain

$$z = \frac{L_3 + L_2}{R_2} \quad \text{and} \quad 0 \le r \le \frac{R_3}{R_2}$$
$$\frac{\partial u_r}{\partial z} = \frac{\partial u_\theta}{\partial z} = \frac{\partial u_z}{\partial z} = 0, \quad \frac{\partial T}{\partial z} = 0 \tag{14}$$

A comment regarding the open ended boundary conditions, 7 and 8, would probably be appropriate here. With the numerical scheme (discussed in the next section) used in the present study, we had the following choices to represent the boundary conditions at the open end of the cavity:

$$\zeta = 0$$

$$\frac{\partial \zeta}{\partial n} = 0$$

where ζ is the variable under consideration.

The first condition is based on the fact that the extension of the boundaries beyond the open end of the annulus is so large that the properties of the fluid leaving the cavity approach that of the ambient fluid. The second condition, on the other hand, implies that we go only far enough as to ensure that the gradient of the fluid variables is negligible in a direction normal to the surface. After extensive numerical experimentation, we discovered that to model the open boundary using the first method, we would need a very large computational domain and, thus, the simulation would be very expensive. The second method gives accurate results without the necessity of a very large extension. Therefore, in the present study, we have made use of this method to simulate the open boundaries of the computational domain.

In this work the open boundaries were systematically extended in all directions and the number of extensions necessary for the computational domain to eliminate the effects of the far-field solution on the flowfield and the heat transfer characteristics inside the open cavity and its immediate surroundings were determined. The results have been presented for the number of extensions that were determined from the above procedure. Many numerical runs were done in which several different far-field boundary conditions plus different extensions of the open boundaries were examined. We have determined the number of extensions which are required to make the flow and heat transfer characteristics inside the open ended cavity and in its surroundings invariant.

This completes the formulation of the problem. To solve the set of highly nonlinear, fully coupled governing equations subject to the above boundary and initial conditions, a numerical scheme was employed. This numerical scheme is briefly described below.

D. Numerical Scheme

A Galerkin-based finite-element method was employed to solve the system of differential equations in the present work. This technique is well-described by Gresho et al.[7] The incorporation of this numerical scheme in the finite-element code used is also well-documented.[8]

The continuum domain is first divided into simply shaped regions called elements within each of which the unknown variables are approximated by using a set of interpolation functions. Substituting these basis functions into the governing equations and boundary conditions yields a residual in each of the equations. The Galerkin method of weighted residuals reduces these errors to zero by making them orthogonal to the interpolation functions of each element. This procedure yields a system of equations for each element, which can be written as

$$\bar{M} \frac{\partial \boldsymbol{V}}{\partial t} + \bar{K}(\boldsymbol{V}) \cdot \boldsymbol{V} = \bar{F} \tag{15}$$

To obtain a transient solution, the continuous time derivative needs to be replaced by an approximation for the history of the time dependent variable over a small portion of the problem time scale. In other words, some sort of a time integration scheme is necessary. The result is an incremental procedure that advances the solution in discrete steps of time. The trapezoidal scheme developed by Gresho et al.[7] was used for the time discretization of the governing equations. By an appropriate combination of two common, second-order-accurate integration techniques, the implicit trapezoidal rule (TR), and an explicit Adams-Bashforth (AB) formula, they developed a stable time integration scheme in which the size of the time step can be optimally varied, based solely on temporal accuracy requirements. Since an implicit time integrator has been used in the present case for discretization of the governing equations in time, at each time step a nonlinear system of equations needs to be solved. We have used the Quasi-Newton solution algorithm to solve the nonlinear system at each time step. This algorithm can be shown to be superlinearly convergent and, in practice, its convergence rate approaches that of the Newton-Raphson, while the time for one iteration of Quasi-Newton is typically 10–20% of the time for a Newton-Raphson iteration.

E. Heat Transfer Analysis

The local Nusselt number used in the present investigation is defined by

$$Nu = \frac{\partial T}{\partial n} \tag{16}$$

where n denotes the normal pointing outward from the surface over which the Nusselt number is to be calculated

$$Nu = \frac{\partial\left(\frac{T - T_\infty}{T_1 - T_\infty}\right)}{\partial(n/R_2)} = \frac{-k\frac{\partial T}{\partial n}}{-2\pi k L_2 \frac{T_1 - T_\infty}{\ln(R_2/R_1)}} \frac{2\pi R_2 L_2}{\ln(R_2/R_1)}$$

which is the ratio of the convection heat transfer to the heat transfer by pure conduction between the two cylinders multiplied by a constant factor, given by

$$\frac{2\pi R_2 L_2}{\ln(R_2/R_1)}$$

Therefore, we see that the Nusselt number defined here is proportional to the ratio of the heat transferred by convection to that by pure conduction between the inner and outer cylinders. The local Nusselt number can therefore be evaluated at any location. The mean Nusselt number over a surface of area A is given by

$$\overline{Nu} = \frac{1}{A}\int_A \frac{\partial T}{\partial n}\, dA \tag{17}$$

These definitions of the local and average Nusselt number are used to represent all the heat transfer results in the present study.

III. Results and Discussion

Results presented here are for a hot inner cylinder ($T_1 = 1$), a cold outer cylinder ($T_2 = 0$), and a radius ratio of $R_2/R_1 = 2.5$ and an outer cylinder length to radius ratio of $L_2/R_2 = 0.5$. Air was used as the working fluid ($Pr = 0.7$). The range of physical parameters used in the present study has been obtained from those of an actual aircraft braking housing. The temperatures attained by the axle are of the order of 200–300°F and by using the actual dimensions, we get Rayleigh numbers of the order of 10^6. Results for two cases, hereby referred to as the "full-hub case" (inner cylinder length = outer cylinder length) and "half-hub case" (inner cylinder length = half the outer cylinder length) are presented here. A schematic view of these two cases is shown in Fig. 3. Some of the physical aspects and steady-state results for this problem are presented in Desai and Vafai.[6]

In our study, a fine mesh was used in regions where steeper gradients were expected, i.e., near all the solid walls and near the open end of the annulus. The mesh was made progressively coarser toward the far-field locations because the field variables were not expected to change by a significant amount in this part of the domain. We determined the mesh size and the size of the extended computational domain after extensive numerical experiments. For the full-hub geometry, the basic grid structure consisted of 3968 elements though these had to be increased to 6112 elements for higher Rayleigh numbers. For the half-hub geometry, the basic grid structure consisted of 5184 elements for low Rayleigh numbers, whereas for higher Rayleigh numbers, the grid consisted of 8672 elements. In our analysis, we used eight-noded isoparametric brick elements with trilinear velocity and temperature approximations and a discontinuous pressure approximation. Typically, all the simulations were started with a rather conservative estimate of the time step size (0.01–0.05). We established the proper time step size by carrying out extensive numerical experimentation. This is also necessary to understand the evolution of the flow and temperature fields in the early stages of the flow development. The variable time increment algorithm incorporated in the code varies the time step size automatically as the flow evolves and approaches steady state. The computations were performed on the Cray-YMP Supercomputer at the Ohio Supercomputer Center. The CPU time required on the Cray-YMP Supercomputer for typical converged steady-state solution was approximately 120 min.

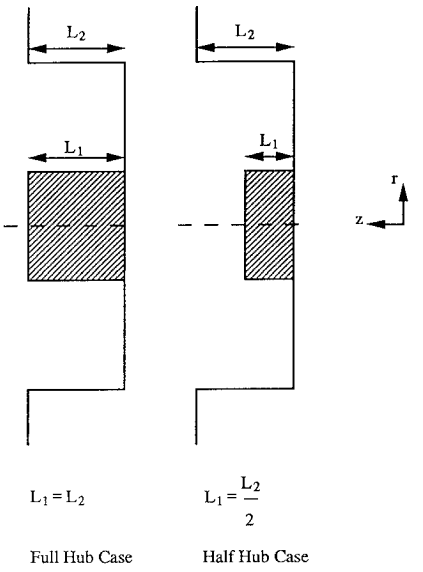

Fig. 3 Schematic representation of the two geometrically different cases.

A. Transient Flowfield and Isotherms

Figure 4 shows the three-dimensional flowfield at the symmetry plane. Results for the flowfield and isotherms are shown in the symmetry plane during the evolution stage at $Ra = 10^6$ to provide an insight into the development process and also the interaction between the inner and outer fluid regions. Also, the formation of the bifurcation zone is clearly understood with the help of these transient results and is the point of emphasis in this section. The display times are chosen such that pertinent information on the flowfield is well-exposed. The corresponding isotherms at the same time steps are shown in Fig. 5. In the early stages of flow development, conduction is the dominant heat transfer mechanism throughout the annulus as indicated by the nature of the isotherms in Figs. 5a and 5b. The isotherms are clustered around the inner cylinder as shown in these figures. During this period, the recirculating flow in the radial planes has not gained enough momentum to transfer energy from the inner cylinder to the other regions of the annulus and the ambient. This is clearly seen from the corresponding flow patterns in Figs. 4a and 4b. The flowfield is characterized by the presence of very weak velocity components.

As time progresses, the flow patterns in Figs. 4c and 4d show that the recirculating flow in the axial direction, as well as the radial planes, has become strong enough to increase the temperature of the fluid in the cavity and its immediate surrounding. From the velocity vector field it can be seen that a relatively stagnant zone begins to appear in the cavity close to the solid end wall. The axial velocity component is very small in this stagnant zone. This is the bifurcation zone which exists in the cavity at high Rayleigh numbers. In the cavity there exist two spiral flow paths, one gushing into the cavity

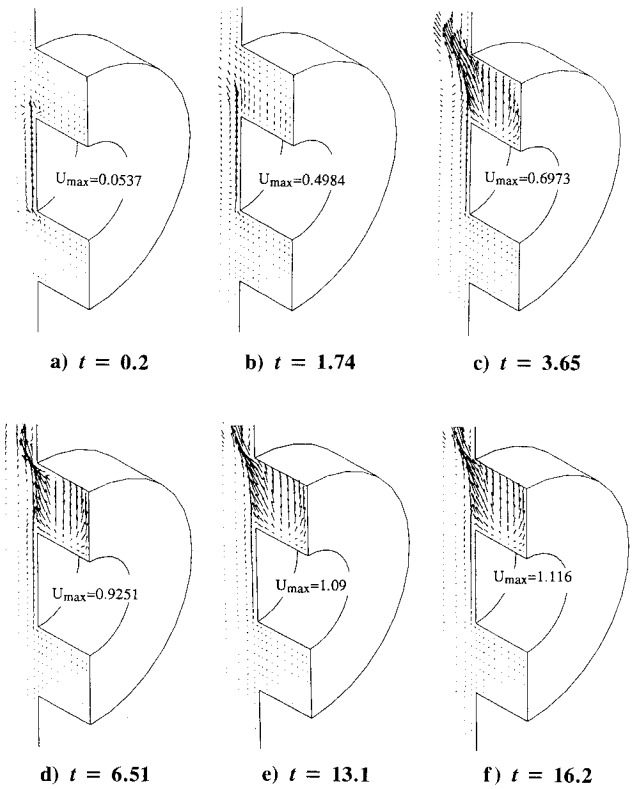

a) t = 0.2 b) t = 1.74 c) t = 3.65

d) t = 6.51 e) t = 13.1 f) t = 16.2

Fig. 4 Velocity vector field in the symmetry plane for $Ra = 10^6$ and different time steps.

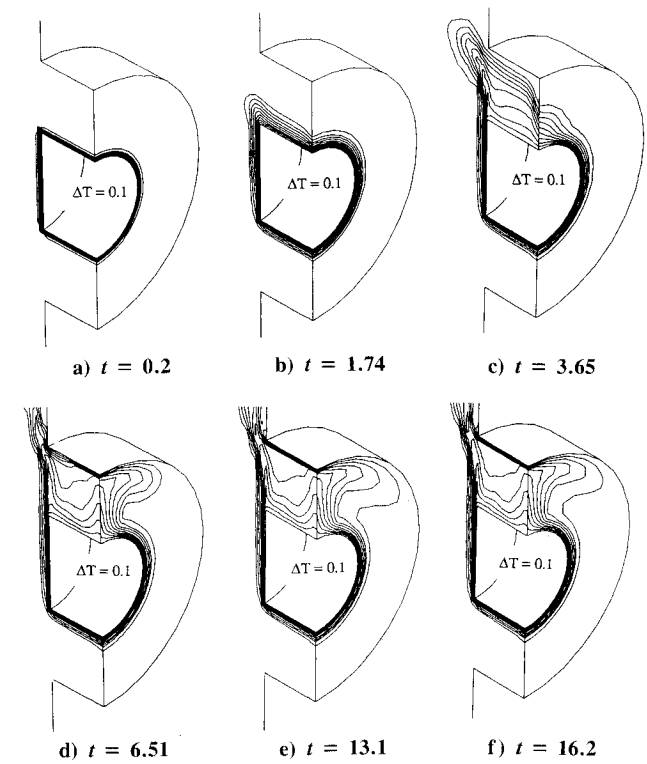

a) t = 0.2 b) t = 1.74 c) t = 3.65

d) t = 6.51 e) t = 13.1 f) t = 16.2

Fig. 5 Three-dimensional view of isotherms for $Ra = 10^6$ and different time steps.

from the ambient surrounding, and the other moving away from the closed end wall and progressively gaining momentum due to reduction of the wall shear effect. The interaction of these two fluid paths causes the formation of the stagnant zone in the cavity. The cavity fluid confined between the bifurcation zone and the closed end wall of the annulus has very little interaction with the surrounding. Fluid interacts with the surrounding only up to the bifurcation zone. At later times this flow pattern stabilizes and reaches a steady-state pattern as shown in Figs. 4e and 4f, which does not change with time.

B. Heat Transfer Results

At steady state, the isotherms for the full hub case at $Ra = 10^4$ and at different positions inside the cavity were compared with the isotherms over the closed end wall of the cavity. As seen in Fig. 6 for almost half of the annulus length starting from the axial end wall, the isotherms are eccentric circles, i.e., they differ only slightly from the pure conduction regime, thereby, indicating the presence of a weak convective flow in the radial planes close to the end wall. The clustering of isotherms around the lower half of the inner cylinder and the upper half of the outer cylinder is a result of the crescent-shaped recirculating flow pattern in the radial planes of the cavity close to the end wall. The axial velocity component, being very weak at these locations, has a relatively lesser influence on the distribution of isotherms. Toward the open end, however, the strong axial flow induced due to the presence of the open boundary coupled with the strong vertical flow, significantly distorts the isotherms in the regions near the aperture plane. The clustering of isotherms around the inner and outer cylinders is more pronounced here than in the regions inside the cavity. The strong axial velocity at the open end causes this concentration of isotherms. The effect of axial convection is maximum at the aperture plane where

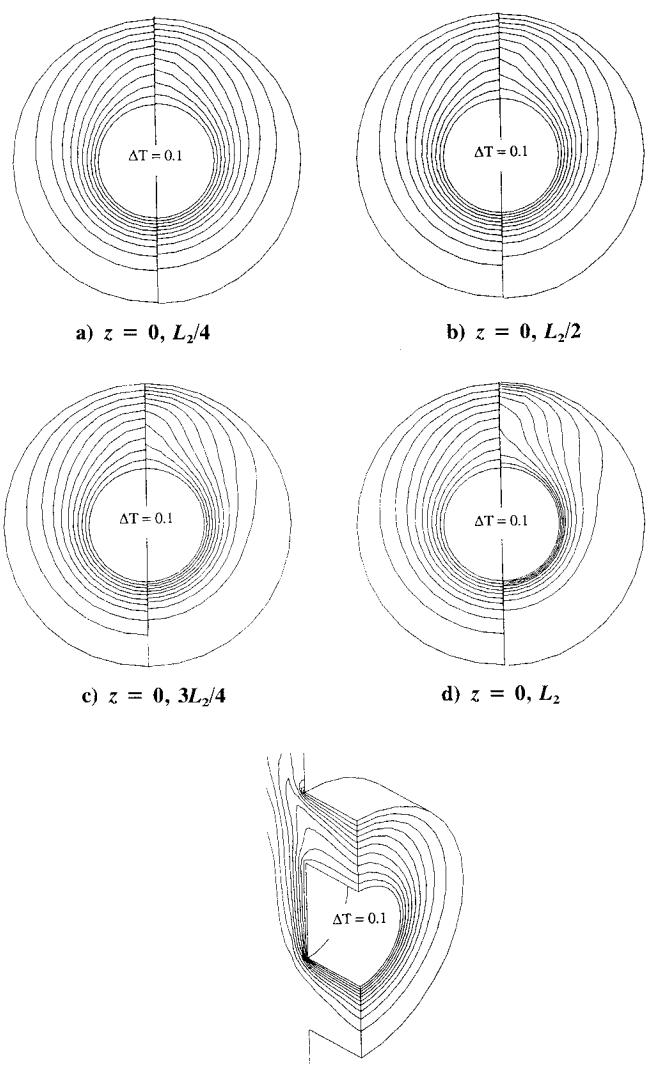

a) z = 0, $L_2/4$ b) z = 0, $L_2/2$

c) z = 0, $3L_2/4$ d) z = 0, L_2

e) Symmetry plane and end wall

Fig. 6 Isotherms for $Ra = 10^4$ (full-hub case).

the magnitudes of the axial velocities are very high. The clustering of isotherms along the vertical (flat) surface of the inner cylinder is a direct result of the strong vertical flow along it. The strong buoyant jet leaving the cavity from the open end results in the concentration of the isotherms along the top half of the outer cylinder as shown in Fig. 6d. The three-dimensional view of the isotherms shown in Fig. 6e also clearly indicates the presence of a strong vertical convective flow in the region immediately outside the annular cavity.

At steady state for the full hub case and at $Ra = 10^6$, an entirely different flowfield results in a considerably different temperature field as shown in Fig. 7. A three-dimensional view of the isotherms shown in the symmetry plane (Fig. 7c) clearly indicates the bifurcated regions inside the cavity. Because of the higher velocities associated with the convective flow in this case, the boundary-layer separation occurs at a location closer to the top of the inner cylinder, and also the very strong buoyant plume impinging on the outer cylinder causes the isotherms to be mostly confined to the upper region of the cavity. Thus, the heat transfer effects are mostly restricted to the upper region of the outer cylinder because the fluid in the lower half, close to the outer cylinder, is virtually stagnant. In Figs. 7a and 7b, isotherms are shown in the same planes which were used to demonstrate the flowfield and are compared with the isotherms at the closed end wall.

The isotherms are clustered around the lower portion of the inner cylinder because of the higher velocities in this region, and around the top portion of the outer cylinder as the buoyant plume strikes it. Also, the clustering of isotherms at the bottom of the inner cylinder is more pronounced because of the higher velocities. Similarly, the clustering of isotherms at the outer cylinder is more pronounced because of the higher impingement velocities in this region. This trend continues until the bifurcation zone where the strength of the convective flow in the radial plane is maximum. At the bifurcation zone, because of the higher velocities in the radial plane, the isotherms are clustered very close to the inner cylinder. This can be seen from Fig. 7c. Beyond this plane, however, the isotherms are less dense around the top portion of the inner cylinder because of a reduction in the strength of the flow in the radial planes. But, because of the higher axial velocities along the outer cylinder, the clustering of the isotherms at the outer cylinder surface is still present. This pattern continues until the open end where, finally, due to the very high velocities, the isotherms are concentrated around almost the entire inner cylinder. The strong convective flow along the heated vertical surface of the inner cylinder is obvious from the clustering of isotherms along this surface. In the top part of the flat surface of the inner cylinder, the clustering of isotherms is significantly less than that in the lower half. This is caused by the strong buoyant jet ejecting from the upper half of the cavity which further enhances the thermal boundary-layer thickness over the vertical flat surface of the inner cylinder.

The transient heat transfer results are explained by considering the time history plots of the mean Nusselt numbers over the inner and outer cylinders as a function of the nondimensional time. Figures 8 and 9 show the transient heat transfer results in the form of time history plots of the mean Nusselt numbers over the inner and outer cylinders. In each figure a comparison is made between the results for the full-hub and half-hub case to understand the effect of the inner cylinder length in heat transfer enhancement. Also, results are presented for the two Rayleigh numbers considered here so that

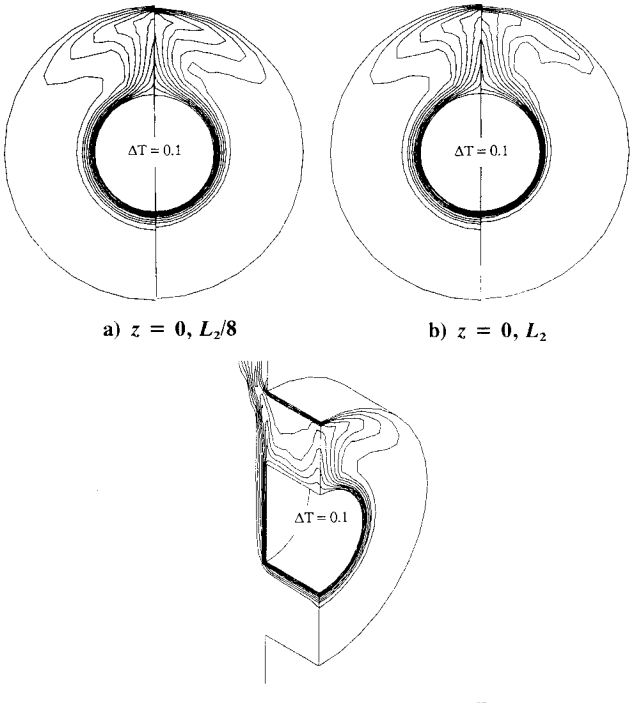

a) $z = 0, L_2/8$ b) $z = 0, L_2$

c) Symmetry plane and end wall

Fig. 7 Isotherms for $Ra = 10^6$ (full-hub case).

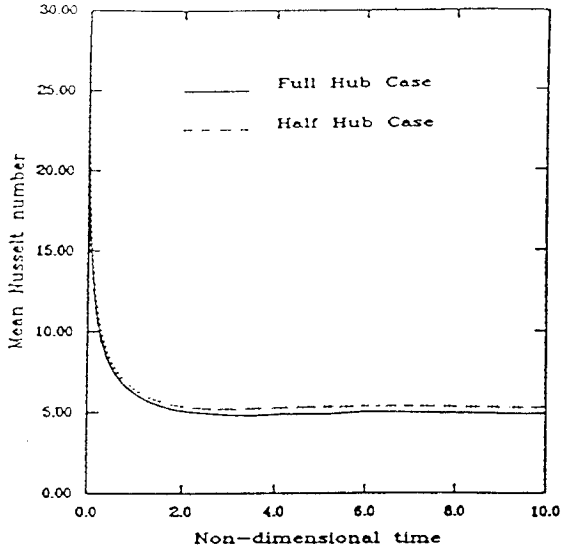

a) $Ra = 10^4$

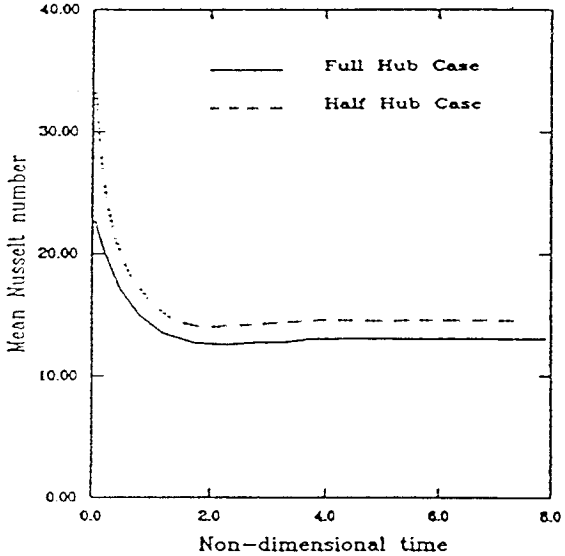

b) $Ra = 10^6$

Fig. 8 Temporal variation of the mean Nusselt number (inner cylinder).

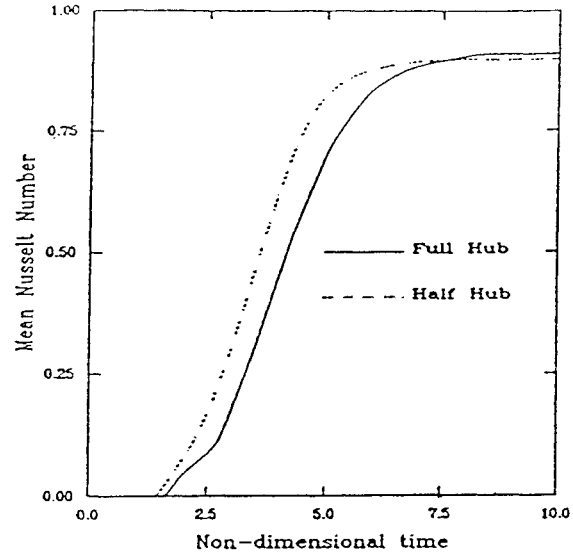

a) $Ra = 10^4$

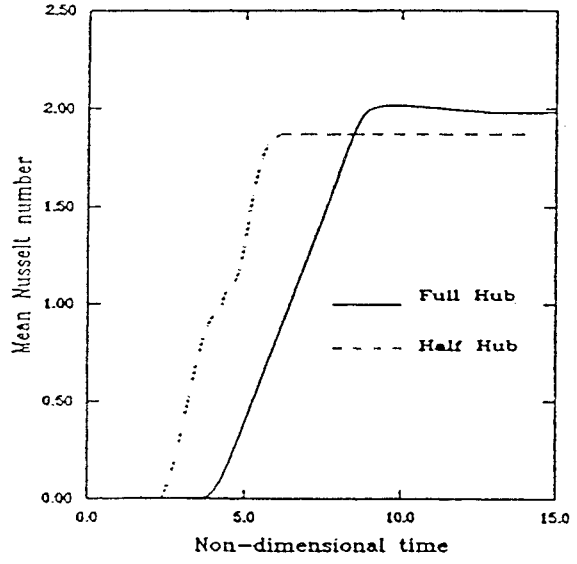

b) $Ra = 10^6$

Fig. 9 Temporal variation of the mean Nusselt number (outer cylinder).

the influence of Rayleigh number on the rate of heat transfer can be analyzed.

Figures 8a and 8b show the time history of the mean value of the inner cylinder Nusselt number for Rayleigh numbers of 10^4 and 10^6, respectively. From these figures, the effect of Rayleigh number in enhancing the heat transfer from the inner cylinder can be easily understood. The steady-state Nusselt number for the full hub case is 5.0 for the lower Rayleigh number and 13.1 for the higher Rayleigh number, therefore, indicating a major heat transfer enhancement. The value of the steady-state Nusselt number for the half hub case is 5.2 for the lower Rayleigh number and 14.0 for the higher Rayleigh number, again indicating a major increase in the heat transfer. Furthermore, it can be seen that the Nusselt number is the highest during the initial evolution stage when the isotherms are clustered around the inner cylinder, resulting in high temperature gradients near the inner cylinder in the initial transient stages of the flow development.

Figures 9a and 9b show the transient results for the outer cylinder mean Nusselt number. In both cases shown, one common feature that can be observed is that the mean outer cylinder Nusselt number for the half-hub case is higher than that for the full-hub case during the initial stages of evolution of the process. However, as the flow approaches steady state, the trend reverses and it is observed that the heat transfer to the outer cylinder is higher for the full hub case. The reason for this feature is as follows. In the initial stages of flow development, the higher local velocities in the cavity for the half-hub case cause the buoyant plume emerging from the surface of the inner cylinder to strike the outer cylinder at higher velocities, thus resulting in higher heat transfer rates. But, in the half-hub case, heat is transferred from a surface (inner cylinder) which has only half the area compared to the full-hub case. This causes a higher total heat transfer from the inner cylinder to the fluid. In both cases, however, the area of the outer cylinder over which heat transfer occurs is equal. This results in a higher heat flux from the outer cylinder in the full-hub case at steady state.

The influence of Rayleigh number on the heat transfer effects can also be seen from the displayed results. The mean Nusselt number has increased by more than 100% due to an increase in Rayleigh number from 10^4 to 10^6. Also, in both cases, the very low Nusselt number (almost equal to zero) during the early stages is explained by the fact that all the activity during the evolution stage is confined to a very thin region around the inner cylinder. Hence, the fluid region close to the outer cylinder is almost stagnant, therefore, resulting in a very low heat transfer to the outer cylinder.

IV. Validity of the Numerical Code

The finite-element code used for obtaining the results in the present study has been verified by Desai and Vafai.[6] Basically, the work consisted of comparing the results obtained from the finite-element code with the numercial and experimental results of previous investigators. Results obtained by Kuehn and Goldstein[9] for a two-dimensional annulus were used for bench marking some of our results. For the three-dimensional annulus with finite length and solid end walls, results were compared with those presented by Vafai and Ettefagh[10] and Takata et al.[2] To avoid repetition, the comparisons are not presented here. For a more detailed comparative analysis, the reader is referred to the paper by Vafai and Desai.[11]

V. Conclusions

The transient buoyancy induced flow and temperature fields in partially open annuli representing the wheel outboard of an aircraft are investigated in this work. A detailed study of the heat transfer characteristics associated with this process has been carried out. The influence of the length of the inner cylinder on the heat transfer characteristics of the annulus has been carefully studied. The numerical results have been obtained for Rayleigh numbers of 10^4 and 10^6. The main results that summarize the contributions of this study are the following:

1) The open end causes a considerable enhancement in the heat transfer in the vicinity of the open end region of the wheel outboard. The numerical results show the complex interactions of the ambient surrounding with the flowfield inside the cavity.

2) The influence of the inner cylinder length on the heat transfer characteristics of the wheel outboard has been investigated. Reduction of the length of the inner cylinder causes higher heat transfer rates from the inner cylinder. At higher Rayleigh numbers, the bifurcation zone is pushed further into the cavity and closer to the end wall, thus causing a better interaction of the ambient fluid with the cavity resulting in an enhancement of the heat transfer from the hub section of the wheel outboard.

Acknowledgment

The grants from BF Goodrich EES 529811 and Ohio Supercomputer Center are acknowledged and greatly appreciated.

References

[1]Ozoe, H., Shibata, T., and Churchill, S. W., "Natural Convection in an Inclined Circular Cylindrical Annulus Heated and Cooled on Its End Plates," *International Journal of Heat and Mass Transfer*, Vol. 24, No. 4, 1981, pp. 727–737.

[2]Takata, Y., Iwashige, K., Fukuda, K., and Hasegawa, S., "Three-Dimensional Natural Convection in an Inclined Cylindrical Annulus," *International Journal of Heat and Mass Transfer*, Vol. 27, No. 5, 1984, pp. 747–754.

[3]Rao, Y., Miki, Y., Fukuda, K., Takata, Y., and Hasegawa, S., "Flow Patterns of Natural Convection in Horizontal Concentric Annuli," *International Journal of Heat and Mass Transfer*, Vol. 28, No. 3, 1985, pp. 705–714.

[4]Ettefagh, J., and Vafai, K., "Natural Convection in Open-Ended Cavities with a Porous Obstructing Medium," *International Journal of Heat and Mass Transfer*, Vol. 31, No. 4, 1988, pp. 673–693.

[5]Vafai, K., and Ettefagh, J., "Thermal and Fluid Flow Instabilities in Buoyancy-Driven Flows in Open-Ended Cavities," *International Journal of Heat and Mass Transfer*, Vol. 33, No. 10, 1990, pp. 2329–2344.

[6]Desai, C., and Vafai, K., "Three-Dimensional Buoyancy-Induced Flow and Heat Transfer Around the Wheel Outboard of an Aircraft," *International Journal of Heat and Fluid Flow*, Vol. 13, No. 1, 1992, pp. 50–64.

[7]Gresho, P. M., Lee, R. L., and Sani, R. L., "On the Time-Dependent Solution of the Incompressible Navier-Stokes Equations in Two and Three Dimensions," *Recent Advances in Numerical Methods in Fluids,* Pineridge Press International, Swansea, Wales, UK, 1980.

[8]*FIDAP Theoretical Manual*, Fluid Dynamics International, Evanston, IL.

[9]Kuehn, T. H., and Goldstein, R. J., "An Experimental and Theoretical Study of Natural Convection in the Annulus Between Horizontal Concentric Cylinders," *Journal of Fluid Mechanics*, Vol. 74, No. 4, 1976, pp. 695–719.

[10]Vafai, K., and Ettefagh, J., "An Investigation of Transient Three-Dimensional Natural Convection in a Horizontal Annulus," *International Journal of Heat and Mass Transfer*, Vol. 34, No. 10, 1991, pp. 2555–2570.

[11]Vafai, K., and Desai, C., "A Comparative Analysis of the Finite Element and Finite Difference Methods for Simulation of Buoyancy Induced Flow and Heat Transfer in Closed and Open Ended Annular Cavities," *Numerical Heat Transfer* (to be published).